Available online at www.sciencedirect.com
ScienceDirect
Journal of Sound and Vibration 318 (2008) 1230–1249
JOURNAL OF SOUND AND VIBRATION
www.elsevier.com/locate/jsvi

Vibration and sound radiation of viscoelastically supported Mindlin plates

Junhong Park[a,1], Luc Mongeau[b,*]

[a]School of Mechanical Engineering, Hanyang University, 17 Haengdang-dong, Seongdong-gu, Seoul 133-791, South Korea
[b]Department of Mechanical Engineering, McGill University, 817 Sherbrooke Street West, Montreal, Quebec, Canada H3A 2K6

Received 3 October 2006; received in revised form 23 April 2008; accepted 23 April 2008
Handling Editor: S. Bolton
Available online 11 June 2008

Abstract

Models based on the Mindlin plate theory were developed and used to investigate the vibro-acoustic characteristics of sandwich panels with viscoelastic supports. The Rayleigh–Ritz method was used to predict the vibration response of the plate subjected to distributed random forces with imposed spectral characteristics. Sound radiation efficiency was calculated for each mode, which allowed the radiated sound power spectra to be determined. Timoshenko beam functions were used as the trial functions. This approach ensured a fast convergence rate, which is advantageous for vibration and sound radiation analysis of high-order modes. The optimal support properties for minimum vibration amplitude were determined. Vibration energy dissipation at the edges was found, as expected, to regulate the vibration amplitude. The effects of the plate mechanical properties on the vibration amplitude and sound radiation were investigated. Sound was found to be predominantly radiated by bending deformation of the face materials at low frequencies, and shear deformations of the honeycomb core at higher frequencies.

1. Introduction

Sandwich panels consisting of thin, stiff face materials and a lightweight honeycomb core possess a flexural rigidity that is much larger than that of homogeneous plates of equal mass. The use of composite sandwich panels has expanded, especially in aerospace applications [1]. These structures have recently been used in aircraft fuselages due to their increased stiffness and lower weight, leading to increased fuel efficiency. One disadvantage of composite sandwich panels is their relatively poor sound barrier performance; stiffer and lighter panel feature increased sound radiation efficiency as a result of larger structural wave propagation speeds. This can contribute significantly to increased cabin noise [2–4].

To model the vibro-acoustic behavior of sandwich panels, the influence of shear deformations of the weak core materials must be considered in addition to that of bending deformations typical of classical (Kirchhoff)

*Corresponding author.
E-mail addresses: parkj@hanyang.ac.kr (J. Park), luc.mongeau@mcgill.ca (L. Mongeau).
[1]Tel.: +82 2 2220 0424.

0022-460X/$ - see front matter © 2008 Elsevier Ltd. All rights reserved.
doi:10.1016/j.jsv.2008.04.045

Nomenclature

a_{mn}^{w}, $a_{mn}^{\psi_x}$, $a_{mn}^{\psi_{y,\hat{q}_j}}$, a_{mn} generalized coordinates
$\hat{A}$, $\hat{B}$, $\hat{C}$ complex amplitude of bending waves (m)
A_m, B_m, C_m, D_m, Λ_m beam function coefficients
b frequency parameter
b_r, b_t viscous rotational (N s/rad) and translational (Pa s) damping coefficients
c_a speed of sound in air (m/s)
D_x, D_y, D_{xy} bending stiffnesses (N m)
f frequency (Hz)
G_{pp},G_{ww}, $G_{\psi_x\psi_x}$, $G_{\psi_y\psi_y}$ cross-power spectral densities
$\hat{H}_j$ frequency response function in terms of generalized coordinates
I_b rotary inertia per unit area (kg)
$[\hat{K}]$ modal stiffness matrix (N/m)
l_x, l_y plate dimensions in x- and y-direction (m)
L_s system Lagrangian (J)
M_b mass per unit area of plate (kg/m^2)
$[M]$ modal mass matrix (kg)
$\hat{P}$ acoustic pressure (Pa)
$\hat{S}_r$, $\hat{S}_t$ complex stiffness of rotational (N/rad) and translational spring (Pa)
S_x, S_y shear stiffnesses (N/m)
T_K kinetic energy (J)
v_{av} spatially averaged mean square velocity (m^2/s^2/Hz)
V_P potential energy (J)
$\hat{\mathbf{v}}_j$ jth eigenvector
$\hat{W}_j$, $\hat{\Psi}_j^x$, $\hat{\Psi}_j^y$ modal shape functions
W_r radiated sound power (W/Hz)
X_m, Y_n trial functions for displacements in x- and y-direction
α, β, k_1, k_2, r, s parameters in Timoshenko beam functions
η_j, η_{rj}, η_{tj} loss factors
ξ, ζ normalized spatial coordinates
ν_x, ν_y Poisson's ratios
ρ_a density of air (kg/m^3)
σ_j radiation efficiency of jth mode
Φ_p wall pressure spectral density (Pa^2/Hz)
ψ_x, ψ_y rotations in x- and y-direction
ψ_m^x, ψ_m^y trial functions for rotations in x- and y-direction
ω circular frequency (rad/s)
$\hat{\omega}_j$ complex natural frequency of jth mode (rad/s)

Indices

m, n, p, q, j integer

plate theory [5,6]. Previous studies of the influence of support properties have been limited to bending deformations, and are thus inappropriate for the case of honeycomb structures. Honeycomb materials have highly anisotropic properties. Their elastic modulus is very large, such that the motion of the two face sheets in sandwich constructions may be considered nearly in phase. Shear deformations within the core govern the dynamic response of sandwich panels at high frequencies. Mindlin's theory [7,8] considers the influence of shear deformations and rotary inertia, in addition to bending deformations for plate structural vibration analysis. This method is therefore well suited to investigate the vibration of sandwich panels. Nilsson and Nilsson [9] investigated the dynamic properties of sandwich structures. Fluid loading effects were found to be an important factor because of the lower specific weight of these structures. In situations where the dynamic properties of composite laminates are anisotropic and not symmetric, the vibration analysis requires coupling between bending and stretching deformations to be taken into account [10]. For this, numerical methods such as the finite element method or the boundary element method are typically needed [11,12]. Mindlin's theory is applicable only for plates that are symmetrically laminated [1,13].

The modal parameters of Mindlin plates may be obtained analytically for simply supported boundary conditions. Numerical methods are required for complex boundary conditions. Dawe and Roufaeil [14] used the Rayleigh–Ritz method to calculate the modal parameters of Mindlin plates with free, clamped or simply supported boundaries (geometric boundary conditions). Timoshenko beam functions were used as trial functions. More recent studies have examined the vibration response of compliantly supported Mindlin plates [15–19]. The consideration of more general boundary conditions allows the analysis of structures that are more realistic, and similar to actual installations. The vibro-acoustic properties of sandwitch panels with viscoelastic supports are significantly different from those with idealized, lossless supports [11,12].

In the present study, models for the vibration response and the sound radiation of sandwich panels were developed. The shear deformation and the rotary inertia of the panels were taken into account analytically using Mindlin plate theory. Rectangular plates supported by viscoelastic springs at the four edges were considered. The Rayleigh–Ritz method was used for the vibration analysis using Timoshenko beam functions as the trial functions. The Rayleigh–Ritz method has advantages over finite element or boundary element methods when analyzing structures with a simple geometry. It is less expensive, requires less computational effort, and thus it is more convenient for design optimization and parametric studies. The effects of the support stiffness on the modal properties of the plate were investigated. The forced vibration response and the radiated sound power induced by distributed random excitations were calculated. Parametric studies were performed to investigate the effects of support and plate mechanical properties. The results provide a better understanding of the vibro-acoustic properties of composite sandwich panels. The resulting model may be useful in the design of sandwich panels with better sound barrier properties.

2. Rayleigh–Ritz method for Mindlin plates

Fig. 1 shows a sketch of the sandwich panels considered in this study. Outer and inner face sheets are made of composite materials of large stiffness, separated by a lightweight honeycomb core. The transverse rigidity of the honeycomb core causes the two face sheets to vibrate in phase. Park [20] measured the dynamic properties of such constructions using the beam transfer function method for several different sandwich beams. The results are shown in Table 1. The bending and shear stiffnesses were measured, and found to vary with frequency. The measured wave propagation speeds, shown in Fig. 2, exhibited characteristics typical of Timoshenko beams. The wave speeds smoothly increased with frequency. At low frequencies, the wave speeds were similar to those calculated assuming "classical" beams. At high frequencies, the wave speeds were almost constant due to the shear deformation of the core. In between these two limiting cases, the beam vibrations were influenced by both the bending and the shear vibrations. The wave speed at high frequencies was supersonic for beams made of Nomex honeycomb. The associated critical frequencies, Table 1, were low and consequently sound radiation was significant over a wide frequency range.

Fig. 3 shows a schematic of the viscoelastically supported rectangular plate. A Cartesian coordinate system is used. The normalized spatial coordinates, $\xi = x/l_x$ and $\zeta = y/l_y$, vary between 0 and 1. The motion of the four edges is restrained by translational and rotational springs. The panel is supported by translational springs with stiffnesses s_{t1}, s_{t2}, s_{t3}, and s_{t4} along the boundaries at $y = 0$, $y = l_y$, $x = 0$, and $x = l_x$, respectively.

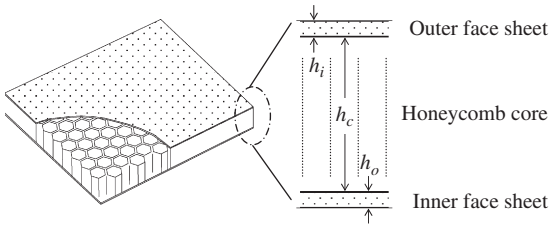

Fig. 1. Schematic of a sandwich honeycomb panel.

Table 1
Mechanical properties of sandwich beams constructed using different core materials

Beam no.	Mass per unit length (kg/m)	Rotary inertia per unit length (10^{-6} kg m)	Bending stiffness (N m^2)	Shear stiffness (kN)	Critical frequency (Hz)
1 (Nomex honeycomb core)	0.33	38	750	105	454
2 (Nomex honeycomb core)	0.27	19	422	39	910
3 (Foam core)	0.37	45	946	10.2	–

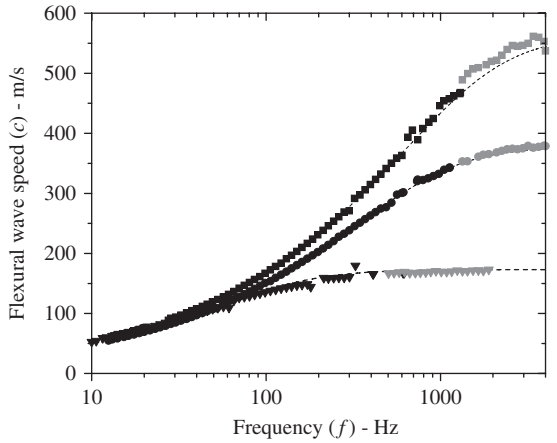

Fig. 2. Flexural wave speeds of the beams and their loss factors: ■, beam 1; ●, beam 2; ▼, beam 3. The dashed lines are calculated values using properties in Table 1.

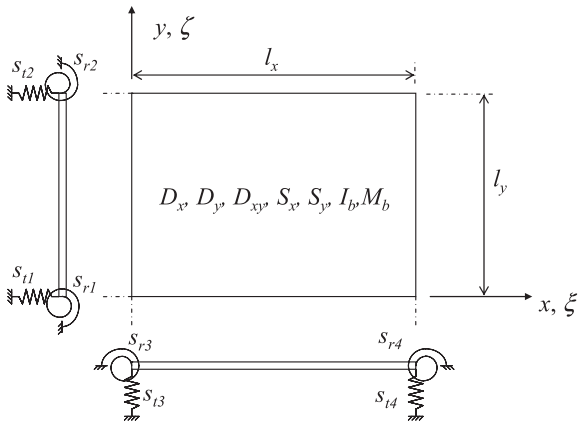

Fig. 3. Geometry of the rectangular Mindlin plate (top view) and its supports (in elevation).

Rotational springs with stiffness, s_{r1}, s_{r2}, s_{r3}, and s_{r4} are arranged in a similar fashion. These springs have stiffness uniformly distributed along each edge.

2.1. Variational formulation—free vibration analysis

Analytical procedures for Mindlin plates are similar to those for homogeneous thin plates [5,6]. The kinetic and potential energy of the Mindlin plate are given as [15]

$$T_K = \frac{1}{2}\int_0^{l_x}\int_0^{l_y} I_b\left\{\left(\frac{\partial\psi_x}{\partial t}\right)^2 + \left(\frac{\partial\psi_y}{\partial t}\right)^2\right\} + M_b\left(\frac{\partial w}{\partial t}\right)^2 \mathrm{d}y\,\mathrm{d}x, \tag{1a}$$

$$V_P = \frac{1}{2}\int_0^{l_x}\int_0^{l_y} D_x\left(\frac{\partial\psi_x}{\partial x}\right)^2 + D_y\left(\frac{\partial\psi_y}{\partial y}\right)^2 + (v_y D_x + v_x D_y)\frac{\partial\psi_x}{\partial x}\frac{\partial\psi_y}{\partial y} + D_{xy}\left(\frac{\partial\psi_x}{\partial y} + \frac{\partial\psi_y}{\partial x}\right)^2 + S_x\left(\frac{\partial w}{\partial x} - \psi_x\right)^2 + S_y\left(\frac{\partial w}{\partial y} - \psi_y\right)^2 \mathrm{d}y\,\mathrm{d}x$$

$$+\frac{1}{2}\left[\int_0^{l_x} s_{t1}w(x,0,t)^2+s_{t2}w(x,l_y,t)^2+s_{r1}\psi_y(x,0,t)^2+s_{r2}\psi_y(x,l_y,t)^2\,\mathrm{d}x\right.$$
$$\left.+\int_0^{l_y} s_{t3}w(0,y,t)^2+s_{t4}w(l_x,y,t)^2+s_{r3}\psi_x(0,y,t)^2+s_{r4}\psi_x(l_x,y,t)^2\,\mathrm{d}y\right], \tag{1b}$$

where w is the vertical displacement, ψ_x and ψ_y are the angular displacements in the x- and y-direction, M_b is the mass and I_b is the moment of inertia per unit area, D_x, D_y, D_{xy} and S_x, S_y are the bending and shear stiffnesses, v_x and v_y are Poisson's ratios. The material properties of the sandwich panel were assumed to be orthotropic. The plate bending and shear stiffness are obtained using as the relations $D_x = E_x h_c^2 h_i/2$ and $S_x = G_c h_c$, respectively. The two face sheets are assumed to be identical, with elastic moduli are E_x. G_c is the shear modulus of the honeycomb core. The dynamic properties of actual composite honeycomb panels depend on several factors such as the composite laminates, the number of layers, the curing process, and the kinds of bonding agents (epoxies) used in their construction. Consequently, their dynamic properties are usually *a priori* unknown and need to be measured using dynamic testing methods [20].

In previous studies [15–19], vertical and angular displacements have been expanded separately, i.e. using expressions of the form

$$\{w(x,y,t),\psi_x(x,y,t),\psi_y(x,y,t)\}=\sum_{m=1}^{N}\sum_{n=1}^{N}\{X_m(x)Y_n(y)a_{mn}^{w}(t),\psi_m^x(x)Y_n(y)a_{mn}^{\psi_x}(t),X_m(x)\psi_m^y(y)a_{mn}^{\psi_y}(t)\}, \tag{2}$$

where X_m, Y_n, ψ_m^x, and ψ_n^y are the trial functions. Distinct generalized coordinates, $a_{mn}^{w}(t)$, $a_{mn}^{\psi_x}(t)$, $a_{mn}^{\psi_y}(t)$, were defined separately for each degree of freedom. In the present study, the vertical and angular displacements were expressed in terms of the same generalized coordinates, a_{mn}, using

$$\{w(x,y,t),\psi_x(x,y,t),\psi_y(x,y,t)\}=\sum_{m=1}^{N}\sum_{n=1}^{N}\{X_m(x)Y_n(y),\psi_m^x(x)Y_n(y),X_m(x)\psi_n^y(y)\}a_{mn}(t). \tag{3}$$

This is required for the estimation of the radiated sound, as shown in a later section. After replacing Eq. (3) into Eq. (1), Lagrange's equation of motion

$$\frac{\mathrm{d}}{\mathrm{d}t}\left(\frac{\partial L_s}{\partial \dot{a}_{mn}}\right)-\frac{\partial L_s}{\partial a_{mn}}=0 \tag{4}$$

is applied, where $L_s = T_K - V_P$ is the system Lagrangian. This yields a set of equations of motion

$$\mathbf{M}\,\ddot{\mathbf{a}}+\hat{\mathbf{K}}\,\mathbf{a}=0, \tag{5}$$

where $\mathbf{M}$ and $\mathbf{K}$ are the mass and stiffness matrices, respectively. Following usual normal mode analysis procedures to calculate the mode shapes and the natural frequencies, the solution of Eq. (5) is assumed to be

$$a_{mn}(t)=\mathrm{Re}\{\hat{a}_{mn}\mathrm{e}^{\mathrm{i}\omega t}\}, \tag{6}$$

where $\hat{a}_{mn}$ is the complex amplitude of a_{mn}. The following eigenvalue problem is obtained:

$$(-\omega^2\mathbf{M}+\hat{\mathbf{K}})\hat{\mathbf{a}}=0. \tag{7}$$

A common approach to model the dissipation of vibration energy was used. The stiffnesses of the supports (Fig. 3) were defined as complex quantities, i.e. $\hat{S}_{tj}=S_{tj}(1+\mathrm{i}\eta_{tj})$ and $\hat{S}_{rj}=S_{rj}(1+\mathrm{i}\eta_{rj})$, $j=1,\ldots,4$. After solving the eigenvalue problem in Eq. (7), the natural frequencies of the plate, $\hat{\omega}_j$, and the associated eigenvectors, $\hat{\mathbf{v}}_j$, were calculated. Note that the eigenvectors are orthogonal because the mass and stiffness matrices are symmetric. The damped natural frequencies, f_j, and the system loss factors, η_j, are related to the complex eigenvalues through

$$\hat{\omega}_j=\omega_j\sqrt{1+\mathrm{i}\eta_j}=(2\pi f_j)\sqrt{1+\mathrm{i}\eta_j}. \tag{8}$$

2.2. Trial functions

Timoshenko beam functions were used as the trial functions. The solution of the Timoshenko beam is well known [21]. The normalized coordinates, ξ and ζ, are used in the calculation of the trial functions. The Timoshenko beam functions in ξ-direction are

$$X_m(\xi) = A_m \sin b_m\beta\xi + B_m \cos b_m\beta\xi + C_m e^{b_m\alpha(\xi-1)} + D_m e^{-b_m\alpha\xi}, \tag{9a}$$

$$\psi_m^x(\xi) = A_m k_1 \cos b_m\beta\xi - B_m k_1 \sin b_m\beta\xi + C_m k_2 e^{b_m\alpha(\xi-1)} - D_m k_2 e^{-b_m\alpha\xi}. \tag{9b}$$

In normalized coordinates, the parameters of the Timoshenko beam functions are given by

$$\begin{pmatrix}\alpha\\ \beta\end{pmatrix} = \frac{1}{\sqrt{2}}\left\{\mp[r^2+s^2] + \left[(r^2-s^2)^2 + \frac{4}{b^2}\right]^{1/2}\right\}^{1/2},$$
$$r^2 = \frac{I_b}{M_b l_x^2}, \quad s^2 = \frac{D_x}{S_x l_x^2}, \quad k_1 = \frac{b(\beta^2-s^2)}{\beta l_x}, \quad k_2 = \frac{b(\alpha^2+s^2)}{\alpha l_x}. \tag{10}$$

The notation follows closely that used by Huang [21]. The frequency parameter, b, is related to the circular frequency through $b^2 = \omega^2 M_b/D_x$. Four boundary conditions at $\xi = 0$ and 1 were applied:

$$\left(\frac{\partial X_m(0)}{l_x\partial\xi} - \psi_m^x(0)\right) = T_1 X_m(0), \ \left(\frac{\partial\psi_m^x(0)}{\partial\xi}\right) = R_1\psi_m^x(0) \tag{11a,b}$$

$$\left(\frac{\partial X_m(1)}{l_x\partial\xi} - \psi_m^x(1)\right) = -T_2 X_m(1), \ \left(\frac{\partial\psi_m^x(1)}{\partial\xi}\right) = -R_2\psi_m^x(1), \tag{11c,d}$$

where

$$T_1 = \frac{S_{t1}}{S_x}, \quad T_2 = \frac{S_{t2}}{S_x} \quad R_1 = \frac{l_x S_{r1}}{D_x}, \quad R_2 = \frac{l_x S_{r2}}{D_x}.$$

By replacing Eq. (9) into Eq. (11) the characteristic equation is obtained as

$$\begin{bmatrix} K_1 & -T_1 & (K_2-T_1)e^{-b_m\alpha} & -K_2-T_1 \\ -R_1k_1 & -k_1b_m\beta & k_2e^{-b_m\alpha}(b_m\alpha-R_1) & k_2(b_m\alpha+R_1) \\ \cos b_m\beta K_1 + T_2\sin b_m\beta & -\sin b_m\beta K_1 + T_2\cos b_m\beta & K_2+T_2 & (-K_2+T_2)e^{-b_m\alpha} \\ k_1(R_2\cos b_m\beta - b_m\beta\sin b_m\beta) & -k_1(b_m\beta\cos b_m\beta + R_2\sin b_m\beta) & k_2(b_m\alpha+R_2) & k_2e^{-b\alpha}(b_m\alpha-R_2) \end{bmatrix}$$
$$\times \begin{bmatrix} A_m \\ B_m \\ C_m \\ D_m \end{bmatrix} = 0, \tag{12}$$

where $K_1 = b_m\beta/l_x - k_1$, $K_2 = b_m\alpha/l_x - k_2$. Eq. (12) is an eigenvalue problem. This eigenvalue problem was solved numerically to obtain the coefficients, A_m, B_m, C_m, D_m. The resulting beam functions were normalized to satisfy the following orthogonality conditions [21],

$$\int_0^1 X_m X_p + (I_b/M_b)\psi_m^x\psi_p^x d\xi = \delta_{mp}, \tag{13}$$

where δ_{mp} is the Kronecker delta function. Similar numerical procedures were repeated to calculate the trial functions along the ζ-direction—Y_n and $\psi_n{}^y$. Finally, with the trial functions calculated in this section, the

mass and stiffness matrices are obtained as

$$M_{mnpq} = l_x l_y \left(M_b \int_0^1 X_m X_p \, \mathrm{d}\xi \int_0^1 Y_n Y_q \, \mathrm{d}\zeta + I_b \int_0^1 \psi_m^x \psi_p^x \, \mathrm{d}\xi \int_0^1 Y_n Y_q \, \mathrm{d}\zeta + I_b \int_0^1 X_m X_p \, \mathrm{d}\xi \int_0^1 \psi_n^y \psi_q^y \, \mathrm{d}\zeta \right), \tag{14a}$$

$$\begin{aligned} K_{mnpq} = {} & \frac{l_y S_x}{l_x} \int_0^1 \frac{\partial X_m}{\partial \xi} \frac{\partial X_p}{\partial \xi} \, \mathrm{d}\xi \int_0^1 Y_n Y_q \mathrm{d}\zeta + \frac{l_x S_y}{l_y} \int_0^1 X_m X_p \mathrm{d}\xi \int_0^1 \frac{\partial Y_n}{\partial \zeta} \frac{\partial Y_q}{\partial \zeta} \mathrm{d}\zeta + \frac{l_y D_x}{l_x} \int_0^1 \frac{\partial \psi_m^x}{\partial \xi} \frac{\partial \psi_p^x}{\partial \xi} \mathrm{d}\xi \int_0^1 Y_n Y_q \mathrm{d}\zeta \\ & + \frac{l_x D_{xy}}{l_y} \int_0^1 \psi_m^x \psi_p^x \, \mathrm{d}\xi \int_0^1 \frac{\partial Y_n}{\partial \zeta} \frac{\partial Y_q}{\partial \zeta} \, \mathrm{d}\zeta + l_x l_y S_x \int_0^1 \psi_m^x \psi_p^x \, \mathrm{d}\xi \int_0^1 Y_n Y_q \, \mathrm{d}\zeta + \frac{l_x D_y}{l_y} \int_0^1 X_m X_p \, \mathrm{d}\xi \int_0^1 \frac{\partial \psi_n^y}{\partial \zeta} \frac{\partial \psi_q^y}{\partial \zeta} \, \mathrm{d}\zeta \\ & + \frac{l_y D_{xy}}{l_x} \int_0^1 \frac{\partial X_m}{\partial \xi} \frac{\partial X_p}{\partial \xi} \, \mathrm{d}\xi \int_0^1 \psi_n^y \psi_q^y \mathrm{d}\zeta + l_x l_y S_y \int_0^1 X_m X_p \, \mathrm{d}\xi \int_0^1 \psi_n^y \psi_q^y \mathrm{d}\zeta - l_y S_x \int_0^1 \frac{\partial X_m}{\partial \xi} \psi_p^x \mathrm{d}\xi \int_0^1 Y_n Y_q \, \mathrm{d}\zeta \\ & - l_y S_x \int_0^1 \psi_m^x \frac{\partial X_p}{\partial \xi} \, \mathrm{d}\xi \int_0^1 Y_n Y_q \, \mathrm{d}\zeta - l_x S_y \int_0^1 X_m X_p \, \mathrm{d}\xi \int_0^1 \frac{\partial Y_n}{\partial \zeta} \psi_q^y \mathrm{d}\zeta - l_x S_y \int_0^1 X_m X_p \mathrm{d}\xi \int_0^1 \psi_n^y \frac{\partial Y_q}{\partial \zeta} \, \mathrm{d}\zeta \\ & + \frac{v_x D_x + v_y D_y}{2} \int_0^1 \frac{\partial \psi_m^x}{\partial \xi} X_p \mathrm{d}\xi \int_0^1 Y_n \frac{\partial \psi_q^y}{\partial \zeta} \mathrm{d}\zeta + D_{xy} \int_0^1 \psi_m^x \frac{\partial X_p}{\partial \xi} \mathrm{d}\xi \int_0^1 \frac{\partial Y_n}{\partial \zeta} \psi_q^y \mathrm{d}\zeta \\ & + \frac{v_x D_x + v_y D_y}{2} \int_0^1 X_m \frac{\partial \psi_p^x}{\partial \xi} \, \mathrm{d}\xi \int_0^1 \frac{\partial \psi_n^y}{\partial \zeta} Y_q \, \mathrm{d}\zeta + D_{xy} \int_0^1 \frac{\partial X_m}{\partial \xi} \psi_p^x \, \mathrm{d}\xi \int_0^1 \psi_n^y \frac{\partial Y_q}{\partial \zeta} \, \mathrm{d}\zeta \\ & + l_x \int_0^1 X_m X_p \, \mathrm{d}\xi \left[\hat{S}_{t1} Y_n(0) Y_q(0) + \hat{S}_{t2} Y_n(1) Y_q(1) + \hat{S}_{r1} \psi_n^y(0) \psi_q^y(0) + \hat{S}_{r2} \psi_n^y(1) \psi_q^y(1) \right] \\ & + l_y \int_0^1 Y_n Y_q \, \mathrm{d}\zeta \left[\hat{S}_{t3} X_m(0) X_p(0) + \hat{S}_{t4} X_m(1) X_p(1) + \hat{S}_{r3} \psi_m^x(0) \psi_p^x(0) + \hat{S}_{r4} \psi_m^x(1) \psi_p^x(1) \right]. \end{aligned} \tag{14b}$$

3. Vibro-acoustic response to random excitation

3.1. Forced vibration

In Eq. (14), the stiffness matrix is symmetric, and the mass matrix has only diagonal terms. The resulting eigenvectors are orthogonal, such that

$$\hat{\mathbf{v}}_j^{\mathrm{T}^*} \mathbf{M} \hat{\mathbf{v}}_m = \delta_{jm}, \tag{15}$$

where $\hat{\mathbf{v}}_j^*$ is the complex conjugate of $\hat{\mathbf{v}}_j$.

After solving the eigenvalue problem, the plate vertical and angular displacements were re-defined as

$$\hat{w}(x,y,\omega) = \sum_{j=1}^{N^2} \hat{W}_j(x,y) \hat{q}_j(\omega), \ \hat{\psi}_x(x,y,\omega) = \sum_{j=1}^{N^2} \hat{\Psi}_j^x(x,y) \hat{q}_j(\omega), \ \hat{\psi}_y(x,y,\omega) = \sum_{j=1}^{N^2} \hat{\Psi}_j^y(x,y) \hat{q}_j(\omega), \tag{16}$$

where the $\hat{W}_j$, $\hat{\Psi}_j^x$, and $\hat{\Psi}_j^y$ are the modal shape functions given as

$$\{\hat{W}_j(x,y), \hat{\Psi}_j^x(x,y), \hat{\Psi}_j^y(x,y)\} = \sum_{m=1}^{N} \sum_{n=1}^{N} \{\hat{\mathbf{v}}_j(mn) X_m(x) Y_n(y), \hat{\mathbf{v}}_j(mn) \psi_m^x(x) Y_n(y), \hat{\mathbf{v}}_j(mn) X_m(x) \psi_n^y(y)\}. \tag{17}$$

For these modal shape functions, the following orthogonality condition is inferred from the orthogonality conditions (Eq. (15)) for the eigenvectors:

$$\left[M_b \int_0^{l_x} \int_0^{l_y} \hat{W}_j^* \hat{W}_k \, \mathrm{d}x \, \mathrm{d}y + I_b \left(\int_0^{l_x} \int_0^{l_y} \hat{\Psi}_j^{x^*} \hat{\Psi}_k^x + \hat{\Psi}_j^{y^*} \hat{\Psi}_k^y \, \mathrm{d}x \, \mathrm{d}y \right) \right] = \hat{\mathbf{v}}_j^{\mathrm{T}^*} \mathbf{M} \hat{\mathbf{v}}_K = \delta_{jk}. \tag{18}$$

When the shape functions defined in Eq. (17) are used as trial functions, the mass and stiffness matrices are diagonal, and the eigenvalue problem is simplified as

$$(\ddot{q}_j + \omega_j^2 q_j) = F_j, \quad j = 1, \ldots, N^2, \tag{19}$$

where

$$F_j = \int_0^{l_x} \int_0^{l_y} p(x,y,t)\hat{W}_j^*(x,y)\,\mathrm{d}x\,\mathrm{d}y. \tag{20}$$

After solving for the transfer function of the generalized coordinates, the forced vibration response is calculated. When the relationship between neighboring excitations are specified as cross-power spectral densities, the displacement response is calculated as

$$G_{ww}(\mathbf{r}_1,\mathbf{r}_2,\omega) = \sum_{j=1}^{N^2}\sum_{k=1}^{N^2} H_j^*(\omega)H_k(\omega)\hat{W}_j^*(\mathbf{r}_1)\hat{W}_k(\mathbf{r}_2)\int_\Lambda\int_\Lambda \hat{W}_j(\mathbf{s}_1)\hat{W}_k^*(\mathbf{s}_2)G_{pp}(\mathbf{s}_1,\mathbf{s}_2,\omega)\,\mathrm{d}\mathbf{s}_1\,\mathrm{d}\mathbf{s}_2, \tag{21}$$

where Λ is the plate area, G_{pp} and G_{ww} are the cross-spectral densities of the distributed excitations and the displacements, respectively, and $\hat{H}_j$ are the frequency response functions for the generalized coordinates, given as $\hat{H}_j(\omega) = -(-\omega^2 + \hat{\omega}_j^2)^{-1}$ from Eq. (19). Similarly, the rotational responses to random excitations are calculated as

$$G_{\psi_x\psi_x}(\mathbf{r}_1,\mathbf{r}_2,\omega) = \sum_{j=1}^{N^2}\sum_{k=1}^{N^2} H_j^*(\omega)H_k(\omega)\hat{\Psi}_j^{x*}(\mathbf{r}_1)\hat{\Psi}_k^{x}(\mathbf{r}_2)\int_\Lambda\int_\Lambda \hat{W}_j(\mathbf{s}_1)\hat{W}_k^*(\mathbf{s}_2)G_{pp}(\mathbf{s}_1,\mathbf{s}_2,\omega)\,\mathrm{d}\mathbf{s}_1\,\mathrm{d}\mathbf{s}_2, \tag{22a}$$

$$G_{\psi_y\psi_y}(\mathbf{r}_1,\mathbf{r}_2,\omega) = \sum_{j=1}^{N^2}\sum_{k=1}^{N^2} H_j^*(\omega)H_k(\omega)\hat{\Psi}_j^{y*}(\mathbf{r}_1)\hat{\Psi}_k^{y}(\mathbf{r}_2)\int_\Lambda\int_\Lambda \hat{W}_j(\mathbf{s}_1)\hat{W}_k^*(\mathbf{s}_2)G_{pp}(\mathbf{s}_1,\mathbf{s}_2,\omega)\,\mathrm{d}\mathbf{s}_1\,\mathrm{d}\mathbf{s}_2. \tag{22b}$$

To obtain the vibration responses without neglecting the inter-modal terms, the orthogonality of the normal modes simplifies the calculation of the sound radiation and the spatially averaged response. The orthogonality conditions for the normal modes, shown in Eq. (18), allows only the calculation of the sum of the responses, $G_{ww} + G_{\psi_x\psi_x} + G_{\psi_y\psi_y}$. For this summation, the contribution from the rotational inertia of the plate, $G_{\psi_x\psi_x} + G_{\psi_y\psi_y}$, is negligibly small compared with that of the vertical vibration, G_{ww}. Consequently, the orthogonality conditions shown in Eq. (18) can be approximated as

$$M_b\int_0^{l_x}\int_0^{l_y} \hat{W}_j^*\hat{W}_k\,\mathrm{d}x\,\mathrm{d}y = \delta_{jk}. \tag{23}$$

The simpler, approximate orthogonality conditions shown in Eq. (23) yield the following spatially averaged displacement response:

$$\int_\Lambda G_{ww}(\mathbf{r}_1,\mathbf{r}_1,\omega)\,\mathrm{d}\mathbf{r}_1 = \sum_{j=1}^{N^2}\left|H_j(\omega)\right|^2\int_\Lambda\int_\Lambda \hat{W}_j(\mathbf{s}_1)\hat{W}_j^*(\mathbf{s}_2)G_{pp}(\mathbf{s}_1,\mathbf{s}_2,\omega)\,\mathrm{d}\mathbf{s}_1\,\mathrm{d}\mathbf{s}_2. \tag{24}$$

Eq. (24) was applied to calculate the forced vibration response for a distributed loading over the plate specified using cross-power spectral densities. One example of such excitation is the Corcos turbulent wall pressure model [5].

3.2. Sound radiation

Assuming a baffled plate mounted within an infinite rigid planar surface, the far-field complex acoustic pressure is calculated using the Rayleigh integral [22]

$$\hat{p}(r,\theta,\phi) = -\rho_a\omega^2\frac{\mathrm{e}^{-\mathrm{i}k_a r}}{2\pi r}\int_0^{l_x}\int_0^{l_y}\hat{w}(x,y)\mathrm{e}^{\mathrm{i}k_a(x\,\sin\,\theta\,\cos\,\phi + y\,\sin\,\theta\,\sin\,\phi)}\,\mathrm{d}x\,\mathrm{d}y, \tag{25}$$

where k_a is the wavenumber ($k_a = \omega/c_a$) and c_a the speed of sound in air. The far-field assumption requires r to be much larger than the plate dimensions, l_x and l_y. Accordingly, the radiated sound power, W_r, is calculated

as the integral of the far-field acoustic intensity over a hemisphere surrounding the plate, as follows:

$$W_r = \frac{\rho_a \omega^4}{8\pi^2 c_a} \int_0^{2\pi} \int_0^{\pi/2} \int_A \int_A \hat{G}_{ww}(\mathbf{r}_1, \mathbf{r}_2, \omega) e^{ik_a(r_2 - r_1)\cdot(\sin\theta\cos\phi, \sin\theta\sin\phi)} \, d\mathbf{r}_1 \, d\mathbf{r}_2 \, \sin\theta \, d\theta \, d\phi. \tag{26}$$

When the Corcos model is used for the input pressure cross-spectral density, the radiated sound power is calculated, neglecting inter-modal terms, using

$$W_r = \frac{\rho_a c_a l_x l_y}{2} \sum_{j=1}^{N^2} \sigma_j(\omega) |w\hat{H}_j(w)|^2 \int_A \int_A \hat{W}_j(\mathbf{s}_1) \hat{W}_j^*(\mathbf{s}_2) \hat{G}_{pp}(\mathbf{s}_1, \mathbf{s}_2, \omega) d\mathbf{s}_1 \, d\mathbf{s}_2, \tag{27}$$

where σ_j is the radiation efficiency of the jth mode and ρ_a the density of air. For the shape function defined in Eq. (17), the radiation efficiency of the jth mode, σ_j, is calculated as

$$\sigma_j = \frac{k_a^2 M_b}{4\pi^2} \int_0^{2\pi} \int_0^{\pi/2} \left| \int_A \hat{W}_j(\mathbf{r}_1) e^{ik_a(\mathbf{r}_1)\cdot(\sin\theta\cos\phi, \sin\theta\sin\phi)} d\mathbf{r}_1 \right|^2 \sin\theta \, d\theta \, d\phi. \tag{28}$$

To calculate the radiation efficiency, the integration with respect to θ and ϕ was performed using Simpson's 3/8 rule with the integral domain (θ, ϕ) sub-divided into 40×40 equally spaced elements.

For the simulation performed in this study, the excitation over the plate was assumed to be perfectly incoherent, homogeneous, and stationary. In this case, the cross-power spectral densities of the distributed excitation pressures between two locations, $\mathbf{s}_1$ and $\mathbf{s}_2$, is given by

$$G_{pp}(\mathbf{s}_1, \mathbf{s}_2, \omega) = \Phi_p(\omega) \delta(\mathbf{s}_1 - \mathbf{s}_2), \tag{29}$$

where Φ_p is the pressure spectral density. With the loading specified as Eq. (29), the spatially averaged vibration response and radiated sound power is obtained as

$$v_{av} = \frac{1}{l_x l_y} \int_A \omega^2 G_{ww}(\mathbf{r}_1, \mathbf{r}_1, \omega) \, d\mathbf{r}_1 = \frac{\Phi_p(\omega)}{l_x l_y M_b^2} \sum_{j=1}^{N^2} \left| \frac{\omega}{(-\omega^2 + \hat{\omega}_j^2)} \right|^2, \tag{30}$$

$$W_r = \frac{\rho_a c_a \Phi_p(\omega)}{2 M_b^2} \sum_{j=1}^{N^2} \sigma_j \left| \frac{\omega}{(-\omega^2 + \hat{\omega}_j^2)} \right|^2. \tag{31}$$

Assuming that the wall pressure spectral density (Φ_p) is unity over the entire frequency range of interest, the spatially averaged mean-square velocity in octave bands with center, lower, and upper frequency limits of ω_o, ω_1, and ω_2, respectively, is calculated analytically using

$$v_{\omega_0} = \int_{\omega_1}^{\omega_2} v_{av} \, d\omega = \frac{1}{2 l_x l_y M_b^2} \sum_{j=1}^{N^2} \frac{1}{\omega_j^2 \eta_j} \mathrm{Im} \left\{ \hat{\omega}_j \ln \frac{(\hat{\omega}_j - \omega_1)(\hat{\omega}_j + \omega_2)}{(\hat{\omega}_j + \omega_1)(\hat{\omega}_j - \omega_2)} \right\}. \tag{32}$$

4. Results and discussions

4.1. Modal analysis

For verification purposes, the natural frequencies of a homogeneous square plate of side length l, with $D_x = D_y = D = Eh^3/12(1-\nu^2)$, $S_x = S_y = \kappa^2 Gh$, and $D_{xy} = D(1-\nu)/2$, $\nu_x = \nu_y = \nu = 0.3$ where h is the plate thickness and $\kappa^2 = 0.8601$ were calculated. To simulate clamped boundary conditions, the support stiffness was assumed to be $S_t = 10^{25}$ Pa and $S_r = 10^{25}$ N/rad. The results from the Rayleigh–Ritz method using the trial functions defined in Eq. (3), shown in Table 2, are in agreement with results from previous studies [14] both for thin ($h/l = 0.01$) and thick ($h/l = 0.1$) plates, thereby verifying the accuracy of the Rayleigh–Ritz method used in this study.

In the following cases, the dimensions of the honeycomb panel were assumed to be $l_x = 1.57$ m, $l_y = 1.39$ m, the specific mass was $M_b = 3.97$ kg/m^2, and the moment of inertia was $I_b = 0.00035$ kg. Differences between

Table 2

Frequency parameters $\Omega = \omega\sqrt{2(1+\nu)\rho l^2/E}$ for plate clamped on all four edges

		Mode					
		1,1	2,1	1,2	2,2	3,1	1,3
$h/l = 0.01$	Present work	0.1754	0.3575	0.3575	0.5267	0.6401	0.6432
	Ref. [14]	0.1754	0.3576	0.3576	0.5274	0.6402	0.6432
$h/l = 0.1$	Present work	1.600	3.060	3.060	4.322	5.054	5.103
	Ref. [14]	1.594	3.046	3.046	4.285	5.035	5.078

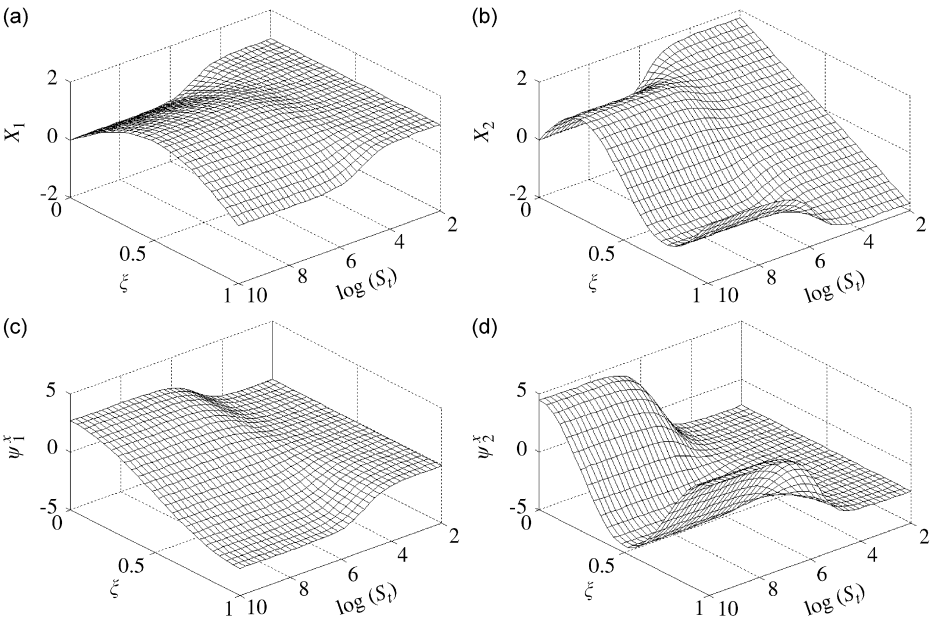

Fig. 4. Effects of translational support stiffness (S_t–Pa) on normalized trial functions of the displacement for (a) $m = 1$, (b) $m = 2$, and the rotation for (c) $m = 1$, (d) $m = 2$.

the dynamic stiffnesses in the x- and y-direction were assumed to be negligible ($D_x = D_y = 8770\,\mathrm{N\,m}$, $S_x = S_y = 513\,\mathrm{k\,N/m}$), and $D_{xy} = 3012\,\mathrm{N\,m}$, $\nu_x = \nu_y = 0.31$. Fig. 4 shows the variation of the four trial functions along the x-direction as a function of translational support stiffness. The first and second trial functions ($m = 1$, 2) are shown. Trial functions for displacement and rotation are shown for both m values. The trial function shapes are similar to the mode shapes of simply supported beams when the translational stiffness is large ($\sim 10^{10}$ Pa). As the translational stiffness is decreased, the trial function shapes approach the mode shapes of free–free beams. In particular, the first ($m = 1$) and second ($m = 2$) trial function shapes approach the mode shapes of translational and rocking rigid-body modes. In between these two extreme cases, the trial function shapes gradually change from the mode shapes of a simply supported beam to those of a free–free beam as the translational stiffness is decreased, as for the classical plate [5].

Dissipation of vibration energy is expected to occur at the edges due to the presence of the viscoelastic supports. The support properties were found to have significant effects on the modal properties and also on the magnitude of the forced response. Fig. 5 shows the change of selected natural frequencies of the plate with support stiffness for $S_r = 0$. The square symbols in the figure show the value where the change rate of the natural frequency with respect to $\log(S_t)$ is maximum. The natural frequencies change from those of a freely supported plate to those of a simply supported plate as S_t is increased. This transition occurs over a limited range of stiffness values in the vicinity of the square symbols. For example, the transition for the fourth

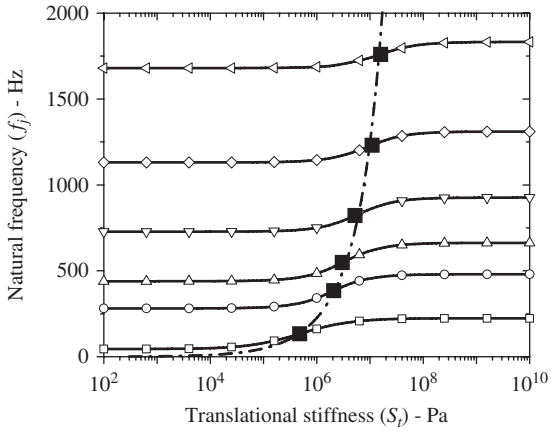

Fig. 5. Effects of translational support stiffness for $S_r = 0$ on the natural frequencies: $-\square-$, f_4; $-\circ-$, f_{14}; $-\triangle-$, f_{24}; $-\triangledown-$, f_{44}; $-\diamond-$, f_{84}; $-\triangleleft-$, f_{164}. The support stiffness predicted from: ▬ · ▬ · ▬, Eq. (38); ■, the values that induces maximum change of natural frequencies with $\log(S_t)$.

natural frequency occurs between $S_t = 10^4$ and 10^7 Pa. This transition zone between free and simply supported behavior occurs at larger values of the support stiffness for higher order modes.

4.2. Radiation efficiencies

Fig. 6 shows radiation efficiencies calculated for various modes of free, simply supported, and clamped plates. The (1,1) and (2,1) modes of the free plate corresponds to the piston and rotational rigid-body motion, respectively. The calculated results are compared with those obtained for the simply supported classical plate [23]. Since the mode shapes of the simply supported classical and Mindlin plates both consist of sinusoidal functions and are identical, the predictions are same for all modes when simply supported. For other boundary conditions, the calculated radiation efficiencies varied with type of structure. In the model, the odd–odd modes radiate sound more effectively than the even–even or even–odd modes at low frequencies. This is because most sound is radiated from the edge following cancelling interferences between adjacent antinodal regions as discussed by Fahy [22].

There are significant differences between the values calculated for the free and the simply supported plates, revealing a significant influence of the translational spring stiffness. In contrast, the calculated values are similar for the simply supported and clamped plates. This implies that the effects of constraining the rotation at the edge are much less significant than those of translational stiffness, as for the classical plate [24]. However, the radiation efficiency of clamped plate was not always larger (for high-order modes) than that of the simply supported plate, which is different compared to those of the classical plate [24]. Fig. 6(b) shows that the clamped plate radiates more effectively than the simply supported one. For higher order modes, as shown in Fig. 6(c), the radiation efficiencies of the clamped plate were smaller than those of the simply supported plate, in contrast to the case in Fig. 6(b).

4.3. Effects of support properties on vibration and sound radiation

The effects of support properties on the forced vibration response were analyzed. Fig. 7 shows the spatially averaged mean square velocity and the radiated sound power as a function of the translational stiffnesses, S_t, for $\eta_t = 0.15$ and $S_r = 0$. For $S_t = 10^2$ Pa, the plate response is analogous to that of a free plate. In this case, sound is radiated mostly by the "piston mode" of vibration as was discussed for classical plates in Refs. [6,24]. The resonance frequencies are readily identified as peaks in the vibration frequency response and the radiated sound power spectra. These resonance frequencies change from those of a freely supported plate to those of a simply supported plate as S_t is increased. A minimum in the spatially averaged velocity and radiated sound

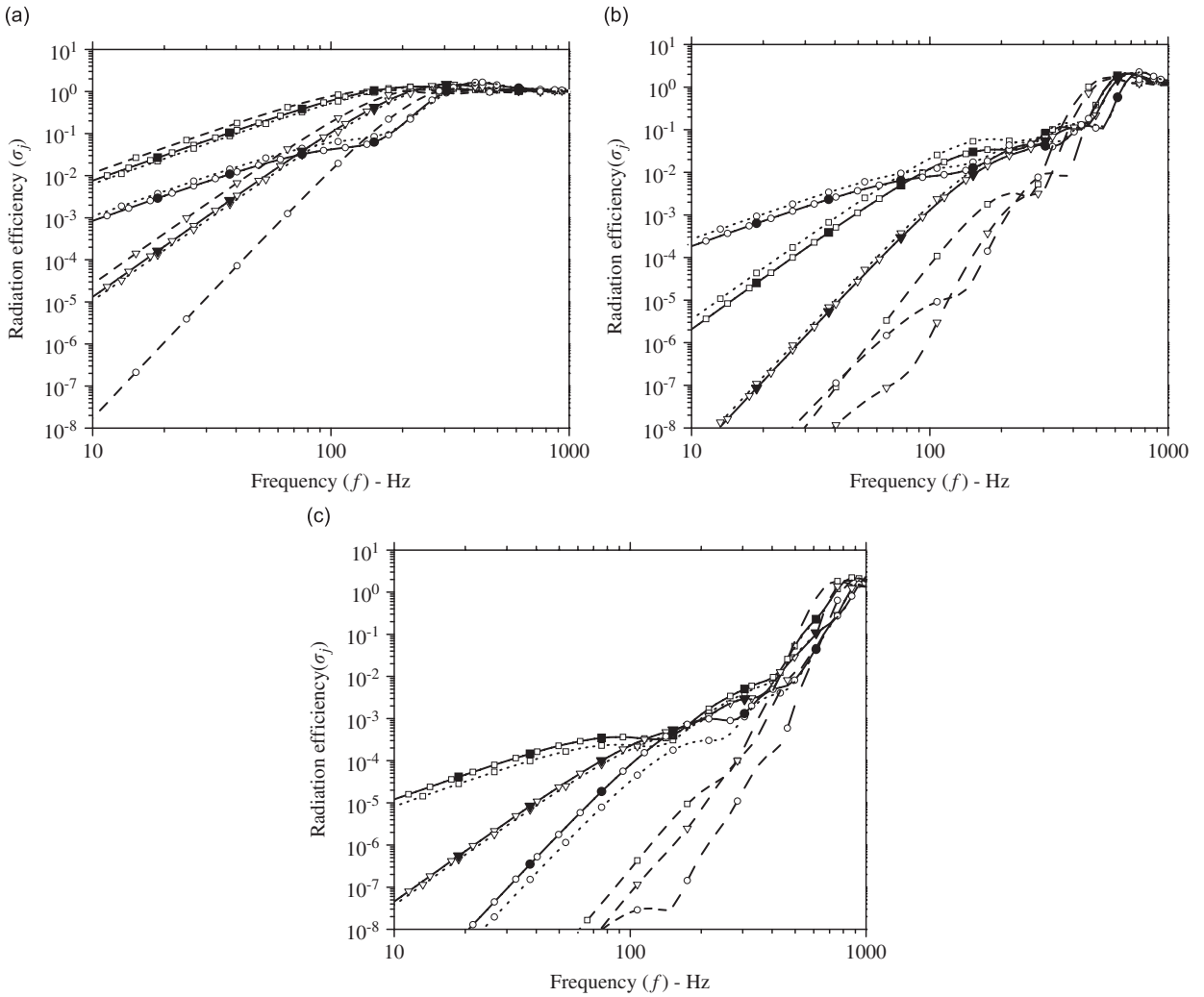

Fig. 6. Radiation efficiency calculated for various modes of free (dashed lines), simply supported (solid lines) and clamped (dotted lines) plates. (a) modes : –□–, (1,1); –▽–, (2,1); –○–, (3,1), (b) modes : –□–, (6,1); –▽–, (6,2); –○–, (7,1), (c) modes : –□–, (5,5); –▽–, (5,6); –○–, (6,6). Filled keys are predictions from Wallace [23].

power spectra, for fixed excitation amplitude, may be identified for intermediate stiffness values. Fig. 8 shows the spatially averaged mean square velocity and the radiated sound power as a function of the rotational stiffnesses. The resonance frequencies change from those of freely supported plates to those of guided plates as S_r is increased. A rigid-body mode that radiate sound like a piston occurs when $S_t = 0$, irrespectively, of the rotational stiffness. In both Figs. 7 and 8, the velocity response was found to be minimal for intermediate values of the complex stiffnesses.

To identify the optimal stiffness values for minimal velocity response, the effects of the support stiffness on the spatially averaged velocity level, calculated using Eq. (32), is shown in octave bands, Figs. 9(a) and (b) which show effects of translational and rotational stiffness, respectively. For each octave band, there is an absolute minimum in the calculated vibration level. The support stiffness that results in this absolute minimum is the optimal value. For verification purposes, the results obtained neglecting shear deformation are also plotted. The results are similar, but the vibration response is greater for the Mindlin plate due to shear deformation, which is neglected in classical plate theory. Fig. 10 shows the predicted vibration response of the plate supported by both translational and rotational springs. The optimal stiffness value for minimal vibration

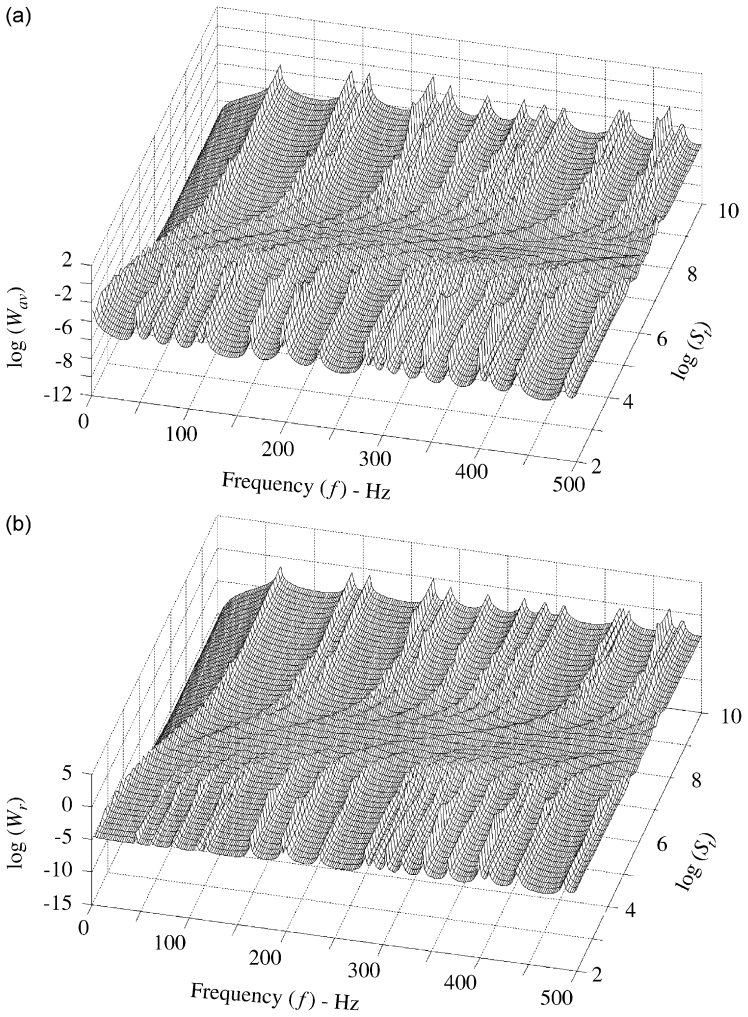

Fig. 7. Dependence of (a) the spatially averaged mean square velocity (v_{av}–m^2/s^2/Hz) and (b) the sound power (W_r–W/Hz) radiated from the plate on the frequency and the support stiffness. $\hat{S}_t = (S_t(1 + 0.15i)$ Pa and $\hat{S}_r = 0$.

response was close to the value calculated for either translational or rotational supports alone. The effects of translational and rotational springs were almost independent from each other. The vibration reduction was more significant when the support translational stiffness was close to the optimal value, especially at high frequencies. These trends are analyzed using simple wave propagation arguments in the following section.

4.4. Wave propagation analysis

One method to investigate the interaction between the plate and the support is to consider wave reflection at boundaries. To determine the wave propagation characteristics analytically, the transverse displacements are assumed to vary only with distance along the direction normal to the edge. In this case, the equation of motion of the flexural vibration is that of the Timoshenko beam, i.e. the one-dimensional equivalent of the Mindlin plate. Fig. 11 illustrates the concept of incident and reflected waves at the edge. To calculate the reflection ratio, normally incident harmonic bending waves with complex amplitude $\hat{B}$ are assumed to propagate toward the edge from $x = \infty$. For the wave propagation shown in Fig. 11, the displacement and rotation are given as

$$w(\xi) = \hat{A}e^{-ib\beta\xi} + \hat{B}e^{-ib\beta\xi} + \hat{C}e^{-b\alpha\xi}, \psi_x(\xi) = -ik_1\hat{A}e^{-ib\beta\xi} + ik_1\hat{B}e^{ib\beta\xi} - k_2\hat{C}e^{-b\alpha\xi}, \quad (33a,b)$$

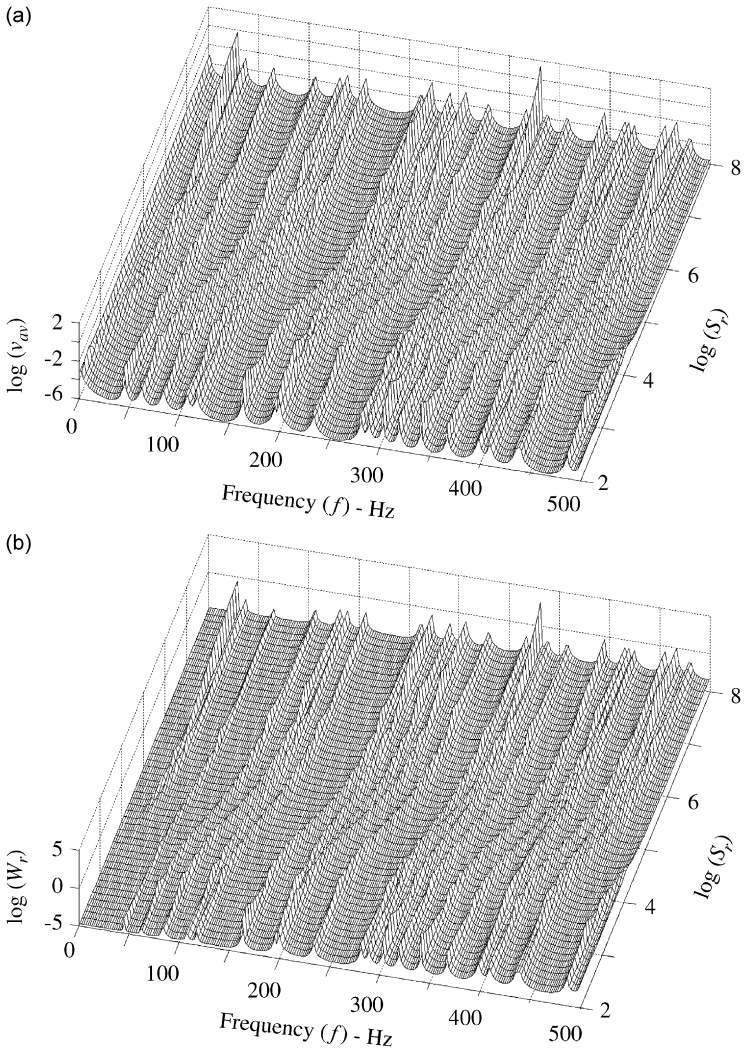

Fig. 8. Same as Fig. 7. $\hat{S}_r = (S_x(1+0.15i)$ N/rad and $\hat{S}_t = 0$.

where $\hat{A}$ and $\hat{C}$ are the complex amplitudes of the reflected harmonic wave and the exponentially decaying wave, respectively. After applying the boundary conditions, Eq. (33), the complex reflection ratios or transfer functions are obtained as

$$\frac{\hat{A}}{\hat{B}} = \frac{b^2\alpha\beta(\mathrm{i}k_2 - k_1) - bk_1k_2(\mathrm{i}\alpha - \beta) - b\hat{T}(\alpha k_2 + \beta k_1) - \mathrm{i}b\hat{R}(\alpha k_1 - \beta k_2) - \hat{T}\hat{R}(\mathrm{i}k_1 + k_2)}{b^2\alpha\beta(\mathrm{i}k_2 + k_1) - bk_1k_2(\mathrm{i}\alpha + \beta) + b\hat{T}(\alpha k_2 + \beta k_1) - \mathrm{i}b\hat{R}(\alpha k_1 - \beta k_2) - \hat{T}\hat{R}(\mathrm{i}k_1 - k_2)}, \tag{34a}$$

$$\frac{\hat{C}}{\hat{B}} = \frac{2\mathrm{i}k_1(b^2\beta^2 - b\beta k_1 + \hat{R}\hat{T})}{b^2\alpha\beta(\mathrm{i}k_2 + k_1) - bk_1k_2(\mathrm{i}\alpha + \beta) + b\hat{T}(\alpha k_2 + \beta k_1) - \mathrm{i}b\hat{R}(\alpha k_1 - \beta k_2) - \hat{T}\hat{R}(\mathrm{i}k_1 - k_2)}. \tag{34b}$$

There is no reflection from boundaries ($\hat{A} = 0$ and $\hat{C} = 0$) when the boundary is supported by viscous elements as in Fig. 11(a), and the damping coefficients are

$$b_t = \frac{S_x(b\beta - k_1)}{\omega} = \frac{D_x b}{\beta\omega}, \quad b_r = \frac{D_x b\beta}{\omega}. \tag{35a,b}$$

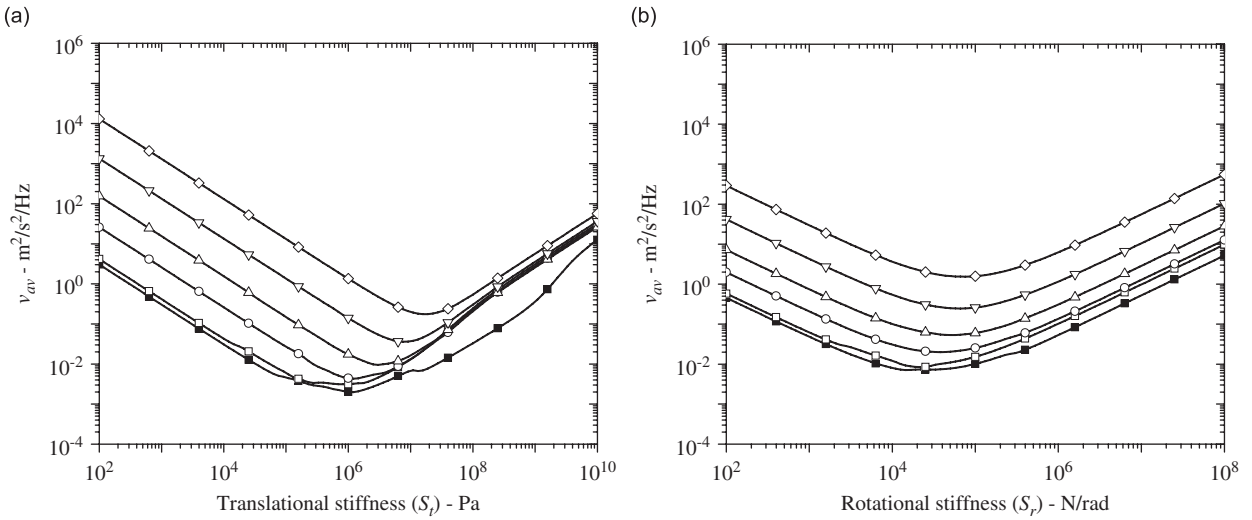

Fig. 9. Effects of the support stiffness on the spatially averaged velocity in octave bands calculated using two different plate vibration analysis—the Mindlin plate theory for center frequencies: –□–, 125 Hz; –○–, 250 Hz; –△–, 500 Hz; –▽–, 1000 Hz; –◇–, 2000 Hz, and the classical plate theory for center frequencies: –■–, 125 Hz. (a) $\hat{S}_t = (S_t(1 + 0.15i)$ and $\hat{S}_r = 0$ and (b) $\hat{S}_r = (S_x(1 + 0.15i)$ and $\hat{S}_t = 0$.

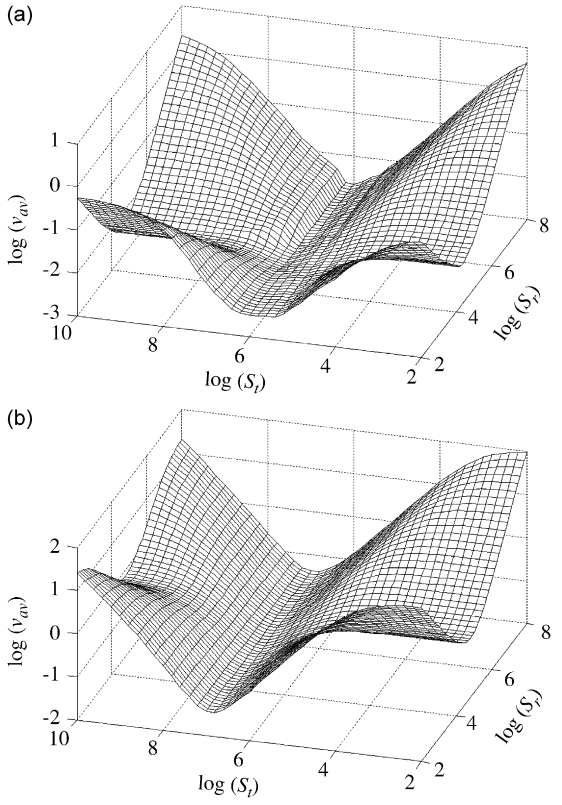

Fig. 10. Effects of the support stiffness, S_t (Pa) and S_r (N/rad), on the spatially averaged velocity (v_{av}—m^2/s^2/Hz) in octave bands of center frequencies: (a) 125 Hz and (b) 1000 Hz.

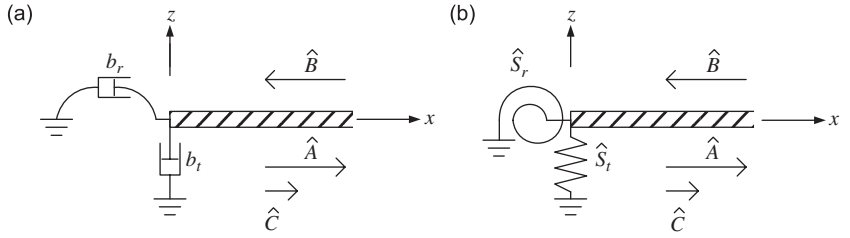

Fig. 11. Normally incident and reflected waves at the edge of a plate: (a) viscous support and (b) viscoelastic support.

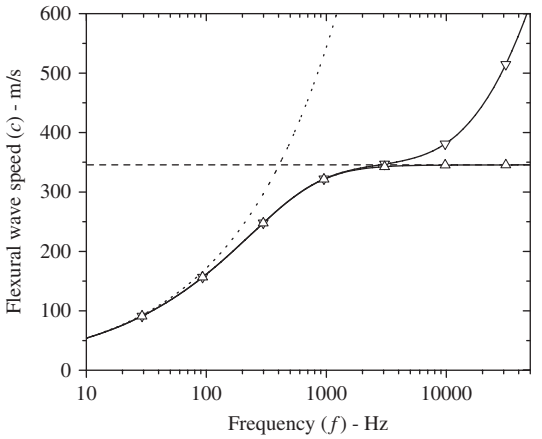

Fig. 12. Calculated speed of flexural waves: $-\triangle-$, Eq. (7); $-\triangledown-$, the method by Kurtze and Watters [25]; $\cdots\cdots$, $c_b = (\omega^2 D_x/M_b)^{0.25}$; $------$ $c_s = \sqrt{S_x/M_b}$.

These damping coefficients are the characteristic impedances of the transverse and rotational vibrations. From the characteristic mechanical impedance of transverse vibrations, the flexural wave speed, c, is derived as

$$c = \frac{b_t}{M_b} = \frac{D_x b}{M_b \beta \omega}. \tag{36}$$

Fig. 12 shows the calculated wave speed for the sandwich panel along with predictions from the method by Kurtze and Watters [25]. The calculated value approaches the shear wave speed, $c_s = \sqrt{S_x/M_b}$, at high frequencies, and the bending wave speed, $c_b = (D_x/M_b)^{1/4}\sqrt{\omega}$, at low frequencies. For the Timoshenko beam, the independent face bending of the face sheets in Kurtze and Watters [25] was not considered. As shown in Fig. 2, the measured wave speeds in honeycomb beams are consistent with values predicted using Eq. (36).

When the honeycomb panel is supported by viscoelastic elements, Fig. 11(b), the restraints from the supports may be idealized by a combination of complex translational and rotational springs. In this case, the boundary stiffness parameters are given by

$$\hat{T} = T(1 + i\eta_t) = \frac{S_t}{S_x}(1 + i\eta_t), \quad \hat{R} = R(1 + i\eta_r) = \frac{S_r}{D_x}(1 + i\eta_r). \tag{37}$$

Fig. 13 shows the calculated dissipation ratio ($= 1 - |\hat{A}/\hat{B}|^2$) vs. support stiffness for $f = 100$ Hz. A fixed loss factor value was imposed, i.e. $\eta_t = \eta_r = 0.15$. The minimal vibration response amplitude is generally obtained when the boundary stiffness minimizes the reflection ratio, and consequently a maximum of energy is dissipated by the support. From the results shown in Fig. 13, the effects of the rotational and the translational support stiffnesses were more or less independent from each other similar to the effects on the vibration response. When a plate supported by translational springs only ($R = 0$) is considered, the optimal support

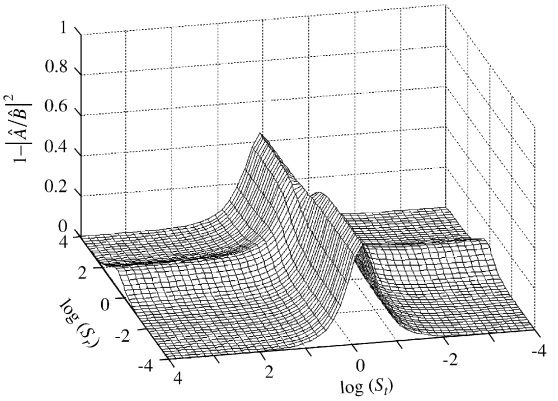

Fig. 13. Effects of support stiffness, S_t (Pa) and S_r (N/rad), on the dissipation ratio of the structural waves when reflected at the edge of the sandwich panel.

stiffness for maximum dissipation ratio is obtained as (for constant loss factor)

$$S_{t,\mathrm{opt}} = S_x \left\{ \frac{b^3 s^4 \left(b^2 r^4 - b^2 r^2 s^2 + 1\right)}{(1 - b^2 r^2 s^2)\left[b^2 (r^2 - s^2)^2 + 4\right]^{1/2} (\eta_t^2 + 1)} \right\}^{1/2}. \tag{38}$$

These stiffness values are very similar to the values for largest rate of change of natural frequencies with respect to logarithm of the support stiffness shown in Fig. 5. This suggests that the maximum dissipation of vibration energy occurs approximately for the same stiffness values as those indicated by squares in Fig. 5. A parallel may be made with the case of the temperature and frequency dependence of the loss factor of typical polymeric material. When plotted as a function of the logarithm of either the frequency or the temperature, the loss factor reaches a maximum value during the transition between the so-called "glassy" state, characterized by a high stiffness, and the so-called "rubbery" state, with a low stiffness [26]. For plates supported by viscoelastic materials, maximum dissipation of vibrational energy occurs during the transition between free and simply supported boundary conditions.

When the plate is supported by rotational springs only ($T = 0$) and the loss factor of the rotational element is fixed, the optimal rotational stiffness for minimum wave reflection is

$$S_{r,\mathrm{opt}} = D_x \left\{ \frac{b(b^2 r^4 - b^2 r^2 s^2 + 1)}{[b^2 (r^2 - s^2)^2 + 4]^{1/2} (\eta_r^2 + 1)} \right\}^{1/2}. \tag{39}$$

The optimal support stiffness that minimized the velocity response was determined from the simulation results for each octave band (Figs. 9(a) and (b)), and is shown in Figs. 14(a) and (b) together with the translational and rotational stiffnesses calculated from Eqs. (38) and (39). The finite size of the plate and the modal response caused slight differences between the two predictions at low frequencies. The agreement is excellent for higher frequency bands which include a larger number of modes.

In many applications, it may be far more convenient to vary the dynamic stiffness, S_t and S_r, by changing the geometry of the support, the material thickness, the contact area, and/or the curvature than to change the loss factor which depends mostly on the support material. Eqs. (38) and (39) should then be used to approximately calculate the optimal support stiffness of the Mindlin plate.

4.5. Effects of plate properties

Figs. 15 and 16 show the spatially averaged mean square velocity and the radiated sound power, respectively, as functions of frequency for three bending and three shear stiffness values. To minimize the effects from the boundary, the boundary translational stiffness was assumed to be very rigid, $S_t = 2 \times 10^{20}$ Pa,

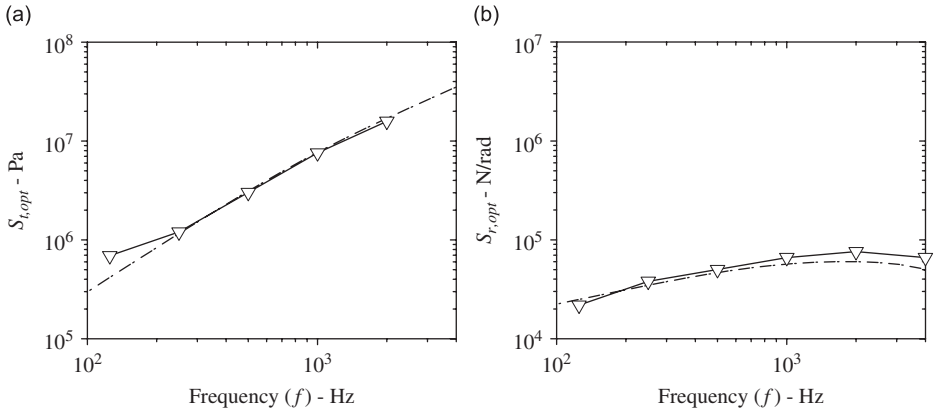

Fig. 14. (a) Optimal translational and (b) rotational stiffnesses calculated for two different methods: –▽–, the minimum spatially averaged mean square velocity; – · – · –, minimum reflections from the edge.

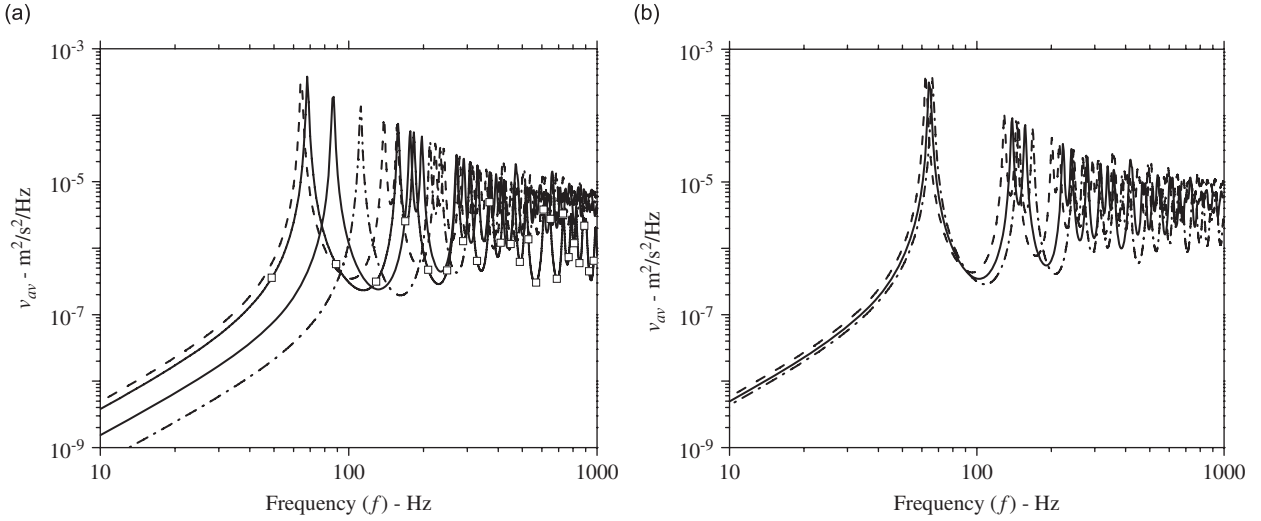

Fig. 15. Spatially averaged mean square velocity vs. frequency for varying dynamic properties—(a) the bending stiffness, D_x: – – – –, 8.8 kN m; ————, 17.5 kN m; – · – · –, 35.1 kN m (Mindlin plate), and D_x: —□—, 8.8 kN m (classical plate); and (b) the shear stiffness, S_x: – – – –, 308 kN/m; ————, 513 kN/m; – · – · –, 1026 kN/m (Mindlin plate).

with $S_r = 0$. A material loss factor of 2% was imposed. At low frequencies, the effects of bending stiffness are significant. As the bending stiffness is increased, the resonance frequencies increase and the velocity response decreases. At higher frequencies, the effects of bending stiffness are minimal, and the effects of the shear stiffness are prominent. An increase in both the shear and bending stiffnesses resulted in a reduced velocity response. In comparison with classical plate models that neglect shear deformation, this resulted in a larger vibration response and increased sound radiation at high frequencies, where shear deformation was dominant. This clearly shows that the shear deformation of the sandwich panel at high frequencies degrades its sound barrier performance.

The effects of the shear stiffness on sound radiation are more complex due to the effects of the radiating wavenumber components. For the case under consideration, the radiated sound power was larger for $S_x = 513$ kN/m than for increased or decreased shear stiffness values, $S_x = 1026$ or 307 kN/m, respectively. When the shear stiffness was initially decreased from $S_x = 1026$ to 513 kN/m, the radiated sound was increased due to the increase in the velocity response. Upon further decrease in the shear stiffness, the resulting decrease in the radiating wavenumber components offsets the increase in velocity response. Consequently, the

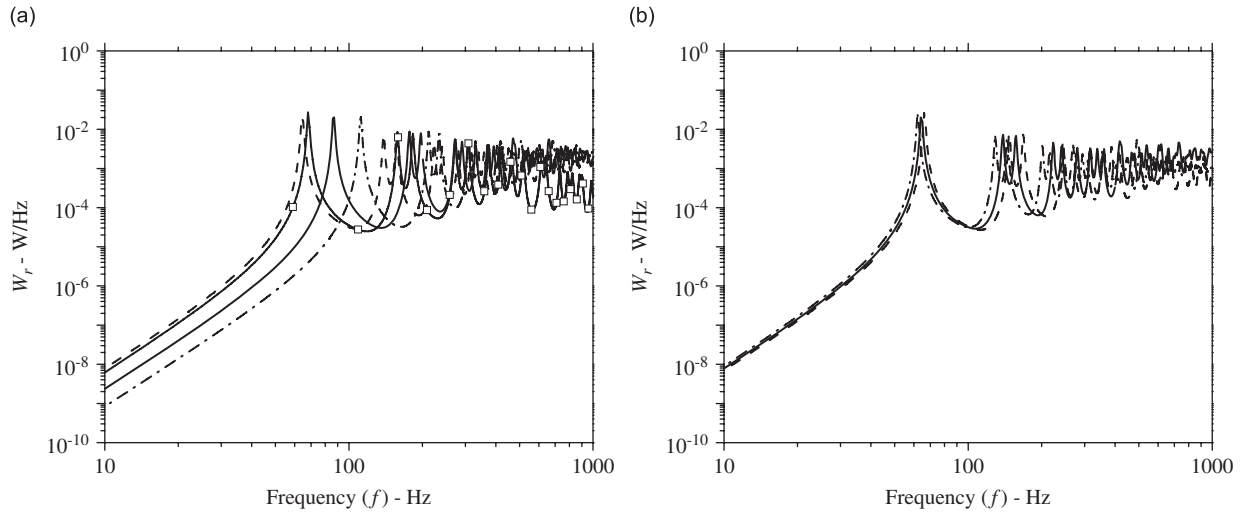

Fig. 16. Radiated sound power vs. frequency for varying dynamic properties—(a) the bending stiffness, D_x: – – – –, 8.8 kN m; ————, 17.5 kN m; – · – · –, 35.1 kN m (Mindlin plate), and D_x: —□—, 8.8 kN m (classical plate); and (b) the shear stiffness, S_x: – – – –, 308 kN/m; ————, 513 kN/m; – · – · –, 1026 kN/m (Mindlin plate).

radiated sound power is reduced. This analysis suggests that shear stiffness values near $S_x = 513\,\text{kN/m}$ would result in the worst possible noise barrier performance for the panel, provided the assumptions of the numerical model are met.

5. Conclusions

The Rayleigh–Ritz method was used to analyze the vibro-acoustic properties of the viscoelastically supported Mindlin plates. Timoshenko beam functions were used as the trial functions. The numerical procedures to calculate modal properties and sound radiation efficiencies were presented, and the effects of support stiffness were investigated. The forced vibration response and the associated free field radiated sound were calculated for randomly distributed excitations. The excitation was assumed to be characterized by its cross-spectral characteristics. The effects of shear deformation within the plate were considered. The optimal support stiffness values for minimal forced vibration response and radiated sound power were found to be in agreement with stiffness values for minimal wave reflection from the edge. Near this optimal stiffness value, the dependence of the natural frequency of the plate on the support stiffness was most pronounced. The effects of the plate mechanical properties on the sound radiation characteristics were also investigated. The radiating wavenumber components increased with increasing plate stiffness, causing increased sound radiation. The inclusion of the shear deformations was shown to be needed in the analysis for sandwich structure models. The results provided insights on the sound generating mechanism, and a better understanding of the factors that may degrade the sound barrier performance of sandwich panel enclosures.

Acknowledgment

This work was supported by the research fund of Hanyang University (HY-2004-S).

References

[1] D. Zenkert, *An Introduction to Sandwich Construction*, Chameleon Press Ltd., London, 1997.
[2] J.S. Mixson, J.F. Wilby, Interior noise, in: H.H. Hubbard (Ed.), *Aeroacoustics of Flight Vehicles, Theory and Practice, Volume 2: Noise Control*, Acoustical Society of America, New York, 1995 (Chapter 16).

[3] E.B. Davis, Designing honeycomb panels for noise control, *Fifth AIAA/CEAS Aeroacoustics Conference and Exhibit*, Bellevue, WA, AIAA Paper 99-1917, May 1999.
[4] H. He, M. Gmerek, Measurement and prediction of wave speeds of honeycomb structures, *Fifth AIAA/CEAS Aeroacoustics Conference and Exhibit*, Bellevue, WA, AIAA Paper 99-1965, May 1999.
[5] J. Park, T. Siegmund, L. Mongeau, Analysis of the flow-induced vibrations of viscoelastically supported rectangular plates, *Journal of Sound and Vibration* 261 (2003) 225–245.
[6] J. Park, T. Siegmund, L. Mongeau, Influence of support properties on the sound radiated from the vibrations of rectangular plates, *Journal of Sound and Vibration* 264 (2003) 775–794.
[7] R.D. Mindlin, Influence of rotary inertia and shear on flexural motions of isotropic, elastic plates, *Journal of Applied Mechanics* 18 (1951) 31–38.
[8] W. Soedel, *Vibrations of Shells and Plates*, Marcel Dekker, Inc., New York, 1993.
[9] E. Nilsson, A.C. Nilsson, Prediction and measurement of some dynamic properties of sandwich structures with honeycomb and foam cores, *Journal of Sound and Vibration* 251 (2002) 409–430.
[10] J.M. Whitney, *Structural Analysis of Laminated Anisotropic Plates*, Technomic Publishing Company, Lancaster, Pennsylvania, 1987.
[11] R.D. Buehrle, J.H. Robinson, F.W. Grosveld, Vibroacoustic model validation for a curved honeycomb composite panel, *Forty-second AIAA/ASME/ASCE/AHS/ASC Structures, Structural Dynamics, and Materials Conference*, Seattle, WA, AIAA Paper 2001-1587, April 2001.
[12] F.W. Grosveld, R.D. Buehrle, J.H. Robinson, Structural and acoustic numerical modeling of a curved composite honeycomb panel, *Seventh AIAA/CEAS Aeroacoustics Conference and Exhibit*, Maastricht, Netherlands, AIAA Paper 2001-2277, May 28–30, 2001.
[13] M.R. Maheri, R.D. Adams, On the flexural vibration of Timoshenko beams, and the applicability of the analysis to a sandwich configuration, *Journal of Sound and Vibration* 209 (1998) 419–442.
[14] D.J. Dawe, O.L. Roufaeil, Rayleigh–Ritz vibration analysis of Mindlin plates, *Journal of Sound and Vibration* 69 (1980) 345–359.
[15] J.H. Chung, T.Y. Chung, K.C. Kim, Vibration analysis of orthotropic Mindlin plates with edges elastically restrained against rotation, *Journal of Sound and Vibration* 163 (1993) 151–163.
[16] J.M. Lee, K.C. Kim, Vibration analysis of rectangular isotropic thick plates using Mindlin plate characteristic functions, *Journal of Sound and Vibration* 187 (1995) 865–877.
[17] J.M. Lee, J.H. Chung, T.Y. Chung, Free vibration analysis of symmetrically laminated composite rectangular plates, *Journal of Sound and Vibration* 199 (1997) 71–85.
[18] D. Zhou, Vibrations of Mindlin rectangular plates with elastically restrained edges using static Timoshenko beam functions with the Rayleigh–Ritz method, *International Journal of Solids and Structures* 38 (2001) 5565–5580.
[19] H. -S. Shen, J. Yang, L. Zhang, Dynamic response of Reissner–Mindlin plates under thermomechanical loading and resting on elastic foundations, *Journal of Sound and Vibration* 232 (2000) 309–329.
[20] J. Park, Transfer function methods to measure dynamic mechanical properties of complex structures, *Journal of Sound and Vibration* 288 (2005) 57–79.
[21] T.C. Huang, The effect of rotatory inertia and of shear deformation on the frequency and normal mode equations of uniform beams with simple end conditions, *Journal of Applied Mechanics* 28 (1961) 579–584.
[22] F. Fahy, *Sound and Structural Vibration: Radiation, Transmission and Response*, Academic Press, London, 1985.
[23] C.E. Wallace, Radiation resistance of a rectangular panel, *Journal of the Acoustical Society of America* 51 (1972) 946–952.
[24] A. Berry, J.-L. Guyader, J. Nicolas, A general formulation for the sound radiation from rectangular, baffled plates with arbitrary boundary conditions, *Journal of the Acoustical Society of America* 88 (1990) 2792–2802.
[25] G. Kurtze, B.G. Watters, New wall design for high transmission loss or high damping, *Journal of the Acoustical Society of America* 31 (1959) 739–748.
[26] J.D. Ferry, *Viscoelastic Properties of Polymers*, Wiley, New York, 1980.